High-resolution MRI of internal field diffusion-weighting in trabecular bone

E. E. Sigmund[1,2], H. Cho[2], Y-Q. Song[2], and E. X. Guo[3]

[1]Radiology, New York University, New York, NY, United States, [2]NMR, Schlumberger, Ridgefield, CT, United States, [3]Biomedical Engineering, Columbia University, New York, NY, United States

Background

Trabecular bone (TB) demonstrates more rapid turnover and has greater import than cortical bone regarding risk of fragility fractures. While the clinically measured bone mineral density (BMD) predicts up to one half of fracture risk, structural properties are also important[1, 2]. Many techniques (MR, CT, ultrasound) exist to incorporate structural information into fracture risk diagnosis. Some MR approaches measure a structurally dependent contrast (e.g. T2'[3, 4], dipolar field[5, 6]), while others image the trabecular structure directly at high resolution[7], often involving specialized coils and postprocessing for 100 μm resolution[8]. Recent work[9, 10] has demonstrated an MR method for TB that has been widely applied to porous media and does not require microimaging. This method probes the magnetization decay from diffusion in the internal field (DDIF)[11]. In a case study of 18 excised bovine tibiae at 2 T, DDIF was shown to scale with the projected surface-to-volume ratio along the applied field, primarily because the largest internal gradients occur near perpendicular trabecular surfaces to the field. This sensitivity was confirmed through comparison with PFG time-dependent diffusometry and μCT image processing. These experiments were not spatially resolved, since their intended purpose is a standard (~1 mm) resolution clinical scan. The present work supports the previous measurements' qualitative picture with DDIF and T1 microscopic imaging.

Methods

Imaging experiments were performed on two excised, cleaned, water-saturated normal bovine TB tibiae samples (length 8 mm, diameter 6 mm). One sample was strong and plate-dominated (Young's modulus 4.5 GPa, bone volume fraction 33%) while the other was an entangled rod/plate structure (YM 0.97 GPa, BVF 17%). The samples were placed in a 7 mm ID glass NMR tube between two susceptibility matching plugs (Wilmad Glass). A 2 T superconducting magnet (Nalorac Cryogenics) with a Bruker Paravision console was used with the applied field along the cylindrical, load-bearing axis. A slice-selective stimulated echo sequence (STE) with 2D spin-warp imaging (Fig. 1a) was used for DDIF contrast. The encoding time t_e was 30 ms, and the diffusion time t_D was varied between 20 ms and 3 s. In each voxel of the images, a single exponential decay was fit to the data resulting in a DDIF decay rate map. A 2D spin-echo imaging sequence (Fig. 1b) was used at variable repeat time TR to map the spin-lattice relaxation rate T_1^{-1}. TR was varied between 50 ms and 15 s, and the magnetization recovery data in each voxel was fit to the steady-state magnetization expression with three adjustable parameters (T_1^{-1}, M_0, θ). These scans were run under 3 different protocols, as illustrated in Figure 1c : (1) axial slices (1 in each sample), 0.15 x 0.15 x 1.5 mm voxel, 64 x 64 matrix (2) coronal slice (through both slices), 0.15 x 0.15 x 1.5 mm voxel, 128 x 64 matrix, (3) coronal slice, 1.25 x 1.25 x 1.5 mm voxel, 16 x 8 matrix. The latter configuration was executed to simulate typical clinical scanner resolution.

Results

Figure 2 shows the results of this imaging study. DDIF images at short evolution time (t_D = 20 ms), dominated by spin density contrast, are shown to indicate the (dark) trabeculae; these structures are consistent with μCT images on these samples. Maps of the spin lattice relaxation rate (T_1^{-1}) and the DDIF decay rate are shown for the corresponding slices. 1D profiles through the centers of these images are shown for each of the three parameters. The T_1^{-1} map shows very little spatial variation in all images. The DDIF map shows high decay rates close to the trabecular walls in both samples and orientations. This correspondence is reinforced by the correlation of DDIF maxima and spin density minima in the 1D profiles. In the low resolution coronal scans, while the trabecular structure is no longer resolved in either sample, the DDIF contrast distinguishes the two samples by a factor of 2 while the spin density and T_1^{-1} maps do not.

Discussion

Prior work has suggested that DDIF probes the projected surface-to-volume ratio of the TB structure, since the internal field gradients are maximized and most abundant close to transverse trabeculae. This claim has been supported by numerous field calculation studies in TB. The image results in Fig. 2 lend further support to this picture, insofar as the DDIF rate is maximized in the proximity of trabecular walls. The anisotropy in the gradient distribution is more difficult to address, given the partial volume averaging over the 1.5 mm slice. Another goal of this study was to enable a feasible DDIF imaging modality. The slice-selective STE approach taken here is reasonably successful, though the slice gradients contribute diffusion weighting that raises the background DDIF rate above the T_1^{-1} limit. Furthermore, histograms of the decay rates show the dependence of the imaging gradients' weighting on slice orientation due to cross terms $\bar{g}_{\text{int}} \cdot \bar{G}_{ext}$. Thus, the next phase of this study will employ a nonselective DDIF sequence filter prior to a fast imaging segment like TSE. Finally, since the water-saturated samples do not show the reduced diffusion or heterogeneity of real bone marrow, this study provides an upper bound for the DDIF contrast in vivo at the same applied field. Higher fields (7 T) should enhance the contrast.

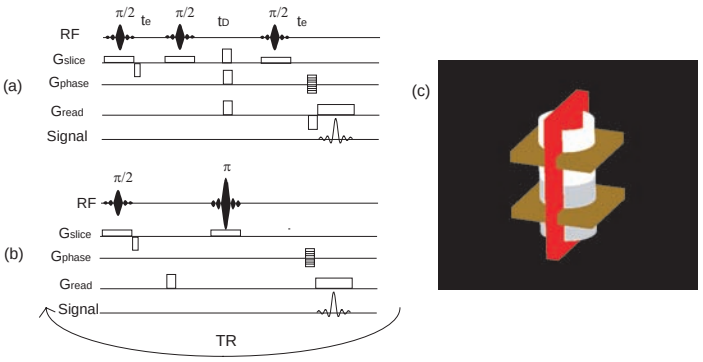

Figure 1: Pulse sequences/slice orientations for (a) DDIF and (b) T_1 imaging. (c) Slice orientations for results shown in Figure 2.

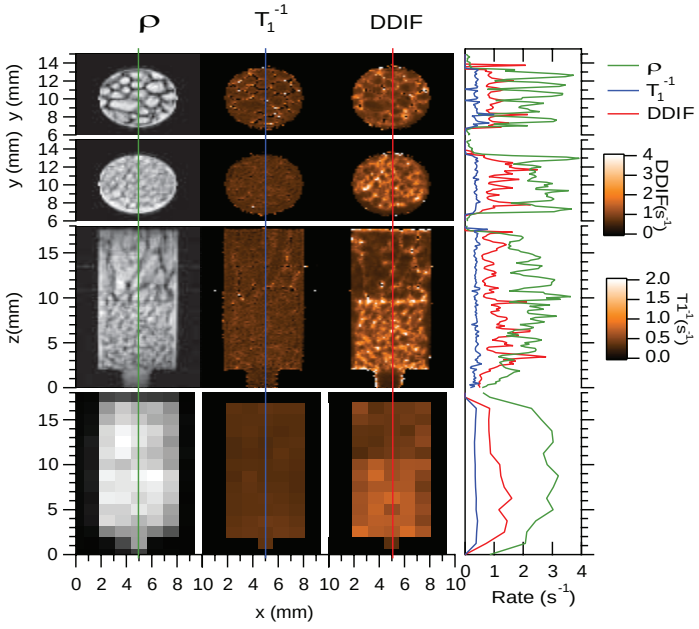

Figure 2: Spin density, T_1^{-1}, and DDIF images for two trabecular bone samples at different slice orientations and resolutions. Right column: 1D profiles along the cylindrical axis through the three image types.

References

[1]Kleerekoper, M., *CTI*, 1985. 37: 594-597. [2]Goldstein, M., *JCP*, 1969. 51: 3728. [3]Engelke, K., *MRM*, 1994. 31: 380-387. [4]Ma, J. *JMR*, 1996. 111: 61-69. [5]Capuani, S., *MRM*, 2001. 46(4): 683-689. [6]Bouchard, L.S., *JMR*, 2005. 176: 27-36.[7]Chung, H.W.,*JBMR*, 1995. 10(10):1452-1461.[8]Hwang,S.N. *MRM*, 2002. 47: 948-957. [9]Sigmund, E.,*Proc. ISMRM*. 2006:1693. [10]Sigmund, E., *MRM*, 2006:under review.[11]Song, Y.-Q., *Nature*, 2000. 406: 178-181.